

Experimental Signatures of Topological Insulators

Laurent LÉVY
Institut Néel
Université Grenoble Alpes and CNRS
BP166
38042 Grenoble cedex 9, France

Abstract. Energy bands in solids describe quantum states in periodic crystals. When a quantum state is wound around the Brillouin zone, it acquires a quantum phase. For a completely filled band, the global phase acquired in this winding is a topological property of the band. For 3D solid with time-reversal symmetry, there are two topological classes corresponding to a ± 1 sign. A signature of topological solids (minus sign) is the presence of conducting surface states with a relativistic dispersion, similar to graphene. They can be observed in angle resolved photo-emission which is able to reconstruct their energy-momentum dispersion below the Fermi level. Some of the experimental signatures of these topological states in strained Mercury-Telluride are presented: their Dirac spectra measured at the SOLEIL synchrotron, the ambipolar sign of their surface charge carriers, the topological phase in their Landau level quantization, and the weak-antilocalization peak in magneto-transport also controlled by the π -topological phase.

1 Introduction

In condensed-matter physics, the quantum mechanical phase is often considered as a fragile quantity subject to thermal fluctuations, disorder or even structural defects. The usual cases when the phase plays a role in macroscopic samples is when the carriers condense in a macroscopic ground state, with the opening of an energy gap which offers a protection against thermal fluctuations.

This is what happens in superconductors, where the electrons condense in a macroscopic BCS quantum state which has a lower energy than the usual electron-Fermi liquid. The phase of the ground state is a macroscopic quantity which is robust and rigid. This phase rigidity against electromagnetic perturbations leads to the Meissner effect expelling a magnetic field from the bulk material.

In low dimensional systems, fundamental symmetries impose definite properties to the quantum mechanical phase, and the usual dephasing processes can be forbidden on symmetry grounds. A classic example is the difference between gapless behavior of half-integer spin-chains which contrast with the gapped structure of integer spin chains, the difference coming from the 4π periodicity of half-integer spin wavefunctions compared to the 2π periodicity of integer spins. The sign difference under a 2π rotation may seem harmless but it kills most quantum fluctuations as the corresponding quantum tunnelling processes become forbidden. The boundaries (end of the chain) define places in space where the symmetries change. This usually

leads to special excitations at the boundaries which are one of the manifestations of a change in the fundamental symmetries.

Topological insulators have stirred a great deal of interest, because there is a symmetry in band structure theory which had not been considered before which leads to similar properties as the one encountered in one-dimensional magnets. The key difference is of course that the symmetry induced by the properties of the quantum phase become truly macroscopic and can indeed be observed in two (quantum spin-Hall effect) and three dimensions (Dirac matter at surfaces).

The problem of topological band structure in solid is illustrated in Fig. 1, [1, 2] where we compare the electronic wave functions and the band structure of solid Neon or Argon, which are atomic insulators with the one of 2D electronic gases in large field. For atomic insulators, the possibilities of hopping between sites are limited by the large splitting between filled atomic shells. Ignoring hopping, all electrons in the filled band have the same shell energies and no low-energy excitations are possible: these solids are indeed strong band insulators with no electrical conductivity. This situation is reminiscent of what happens in a 2D electron gas, where all the electrons condense in Landau level where they have all the same energies. Provided that the chemical potential lies between Landau levels, these macroscopic states are filled and no low energy excitations are available: indeed the bulk longitudinal conductivity is zero. However, in 2D quantum Hall systems, there are n -edge states forming at the boundaries which signals that there is a fundamental symmetry change between the interior of the 2D system and vacuum: the consequence is a finite Hall conductivity $\sigma_{xy} = n \frac{e^2}{h}$, directly related with the number of edge states at the boundary. The index n is in fact the difference between two topological indices, the index of the 2D quantum Hall state (n) and the one of vacuum (0).

This difference between atomic insulators and quantum-Hall states shows that all the information is not simply contained in the energy spectrum, but that the ground state wavefunction and more specifically its phase matters and leads to macroscopic differences, here in the Hall conductivity σ_{xy} .

The notion of Brillouin zone (or magnetic Brillouin zone for quantum Hall systems) is essential to understanding how topological quantum numbers may arise in solids. There is a natural atomic periodicity in 3D crystalline solids, which allows to identify quantum states with a wavevector q_x in the \hat{x} direction with a state with wavevector $q_x + m \frac{2\pi}{a}$ where a is the lattice periodicity in the x direction. This means that only states with wave-vectors in the range $[-\frac{\pi}{a}, \frac{\pi}{a}]$ need to be considered. Since the states at $-\pi/a$ and π/a are identical, the Brillouin zone has the topology of a torus. Suppose now that by applying an electric field for a finite time in this same direction \hat{x} , we take a quantum state from q_x to $q_x + \frac{2\pi}{a}$, i.e. one makes a closed loop around one of the Brillouin zone section of the torus. The final state being the “same” as the initial state, it can only differ by a phase factor after this winding around the Brillouin zone section. In general this phase depends on the specific way, it was wound across the Brillouin zone. However if we repeat the operation for the wavefunction of all the electrons in a filled band, the overall phase acquired by this wavefunction can only take two values 2π or π for a 3D solid with time-reversal symmetry. It is in fact time reversal symmetry which imposes this phase factor to be real, leaving ± 1 as the only possible values. This amounts to a sign change in the filled band wavefunction when winding around the Brillouin zone. Since there are

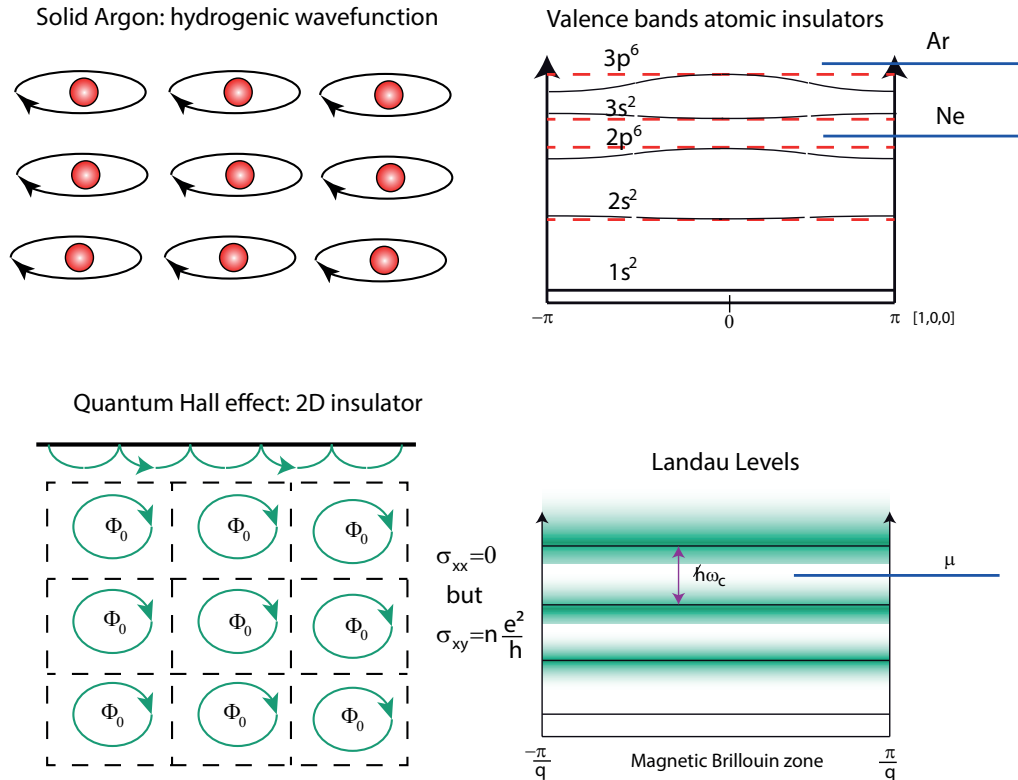


Figure 1: Different solids, may have the same band spectra, but different electronic properties. In an atomic solid, such as solid neon or solid argon, atomic shells are filled and the corresponding bands have little dispersion. The chemical potential of such atomic solid lies in between filled and empty bands and there is no electronic transport possible as thermal excitation cannot excite electrons across the shell gaps. A two-dimensional electron gas in a magnetic field has a similar spectrum, and when the chemical potential lies in between Landau levels, the longitudinal conductivity is zero. In this quantum Hall regime, the system has a quantized Hall conductivity in units of $\frac{e^2}{h}$, where n is the number of edge states. The presence of gapless excitations at the boundaries is a signature of a change of symmetry, here a topological symmetry class.

usually several filled band in a 3D solid, the signs corresponding to all the filled bands have to be compounded. This gives one of the procedure defining the topological index of a band-insulator: since it is just sign the overall symmetry is Z_2 . When the sign is $+1$, the material is an ordinary insulator, while the -1 sign describe the new class of topological insulating materials.¹

When the spin-orbit interaction is weak, Fu and Kane [3] showed that the topological index C of a band insulator depends on the number p of P bands below the Fermi level: $C = (-1)^p$. This relation offers a search route for real material that are topological insulators. Any material class where a band inversion between S and P bands takes place will change the value of p by one and turn a band insulator into a topological insulator. There are several materials with a so called negative gap, i.e. with an inverted band structure. Among them, we find Cadmium Telluride (a normal insulator) with a gap $\Delta = 1.51\text{eV}$ between the Γ_6 (S band) and the Γ_8 (P band) and its topological counterpart Mercury Telluride where this gap is negative

¹For three-dimensional insulators, the accumulated phases are additive when wrapping the Brillouin Zone torus on a sphere: the topological index is an integer, with topological symmetry Z .

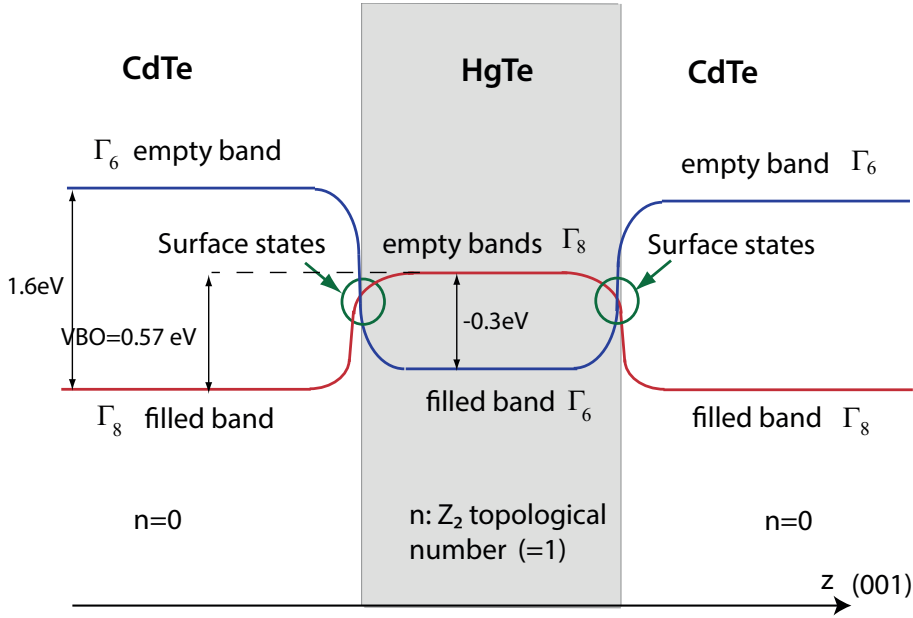


Figure 2: A thick slab of Mercury Telluride is sandwiched between a Cadmium Telluride substrate and cap-layer. The material growth direction is \hat{z} . We consider the center of the Brillouin zone and represent the extrema of the Γ_6 (S band $J = 1/2$) and the $\Gamma_{8,LH}$ ($J = 3/2, m_J = \pm 1/2$). For simplicity, the heavy hole band is not represented. The filled $\Gamma_{8,LH}$ of CdTe and the filled Γ_6 band of HgTe have different topological symmetries and cannot be connected across the interface. On the other hand the filled CdTe $\Gamma_{8,LH}$ band has connects to the empty HgTe Γ_6 band with the same orbital symmetry. The same thing happens between the filled HgTe Γ_6 band and empty CdTe $\Gamma_{8,LH}$ band. These band necessarily cross at the interface, where a gapless surface state appears as a result of the inverted symmetries.

$\Delta = -0.3$ eV (inverted bands). Other pairs of materials with gaps of opposite signs and topologies are $\text{Bi}_{1-x}\text{Sb}_x$ and BiSb .

We now consider two materials with different topological symmetries. The filled band of a topological insulator cannot be connected to an insulator filled band, because they differ by their topological index. Hence as the interface between the two materials is crossed, the only possible correspondence is between a filled valence band and an empty conduction band. Another equivalent argument is that the connection between bands can only involve the same orbital symmetries: the Γ_8 band (P) of HgTe above the Fermi level connects with the filled Γ_8 band in CdTe. This is represented schematically on Fig. 2.

We see that the bands cross at the surface, leading to a metallic surface states. The analogy with edge states in the quantum Hall effects which signal a change in topological class, these surface states signal a change of topological symmetries at the interface and are considered as the hallmark of a material with a nontrivial band topology. Because of Kramer's theorem, the band crossing takes place at one of the symmetry points of the Brillouin zone, usually the zone center. As one moves away from this point into the Brillouin zone, spin-orbit contributions split the Kramer's pair linearly, giving a linear dispersion in crystal momentum k . The presence of a Dirac cone is one of the very distinctive property of topological surface states which can be contrasted with other massive (Shockley [4] and

Tamm [5]) surface states found in condensed matter physics. The states on the Dirac cone emerging from a Kramer doublet are time reversed states: this gives a helical spin structure (the spin of surface charge carrier are tangent to the cone, at least close to the Dirac point). Symmetry arguments do not specify the Dirac point energy, besides the fact that it is between the inverted bands. This complicates the picture significantly because the 3D bulk bands are also present and the interaction between bulk and surface bands can lead to hybridized states. Furthermore, in electronic transport, a ‘pure’ conductivity response coming from the surface states alone are hard to observe, because spurious conduction involving bulk states often contaminates the measured electrical conductivity tensor (σ_{xx} and σ_{xy}).

2 Bulk gap in strained Mercury Telluride

The band structure of Mercury Telluride is shown on Fig. 6. The Γ_8 band being a $P_{3/2}$ band, it is split by spin orbit into $\pm 3/2$ (Γ_{8hh}) (heavy holes) and $\pm 1/2$ (Γ_{8lh}) (light hole) components. The Γ_{8lh} is the conduction band (positive charge carriers) while the Γ_{8hh} is a valence band. In absence of strain, they are degenerate at the zone center (Γ -point). As a result, Mercury-Telluride is a semi-metal with bulk-bands present everywhere in the energy spectrum. The Γ_6 band being 0.3 eV below the Γ_{8lh} , topological surface states can still develop in between, but the coexistence of bulk and surface state is an issue at least in transport experiments. For this reason, it was suggested early on [6] that a strain-gap between the two Γ_8 bands could be open when HgTe is grown on a CdTe substrate which lattice constant ($a_{\text{CdTe}} = 6.48\text{\AA}$) is 0.3% times larger than the one in HgTe ($a_{\text{HgTe}} = 6.46\text{\AA}$). This small lattice mismatch allows to grow homogeneously expanded HgTe layers up to 150 – 250 nm before dislocation spontaneously appears. At such thicknesses, the material is well in the three-dimensional regime. As will be shown in the next section the crossover to the 2D regime occurs between 15 and 25 nm. The 3D-spectrum of the strained layers can be computed using the Kane-model [7] with the Bir-Pikus Hamiltonian [8] and is shown on the left panel of Fig. 6. Although the strain-gap magnitude is small, the only states which are present in this energy interval are the topological surface states (black lines). The only unknown is the actual position of the Dirac point with respect to the top of the Γ_{8hh} valence band and the band velocity (slope).

This information is best obtained using ARPES experiments which measures the energy spectrum of the occupied states in a solid. This technique is particularly suited for probing surface states as the photons penetrate 1nm into the sample, less than the surface states width.

3 ARPES spectra and surface Mercury Telluride

The photon energy used in ARPES experiments is usually in the 15 – 30 eV range, above the material workfunction ($\Phi = 5.8$ eV for HgTe) but below the energy of Mercury and Tellurium core levels. In this range, the relationship between the measured kinetic energy E_{kin} of the extracted electron and the binding energy $E_B(k)$

of its original occupied state is [9]

$$h\nu = E_{kin}(\vec{K}) + \Phi + E_B(\vec{k}), \quad (1)$$

$$\frac{h\nu}{c}\hat{P} = \vec{K} - \vec{k}; \quad (2)$$

\hat{P} is the direction of the incident photon, \vec{K} is the momentum wavevector of the extracted electron in vacuum ($E_{kin} = \frac{(\hbar K)^2}{m}$) while \vec{k} is the crystal wavevector of the electron in the solid. ARPES is a useful technique only when the surfaces are sufficiently clean so that a definite relationship between the crystal wavevector and the (measured) wavevector of the extracted electron can be established. For a pristine surface,

$$k_{\parallel} = K_{\parallel} = \frac{\sqrt{2mE_{kin}}}{\hbar} \sin \theta, \quad (3)$$

$$k_{\perp} = \frac{\sqrt{2m(E_{kin} \cos^2 \theta + V_0)}}{\hbar}, \quad (4)$$

where the crystal wavevector k_{\parallel} parallel to the surface, preserved as the electron crosses the surface, has to be understood in an extended zone scheme (i.e. with the possible addition of a reciprocal lattice wavevector). Here $V_0 = \Phi + E_0$ which is the sum of the workfunction and the energy of the bottom of the band is the “inner” potential.

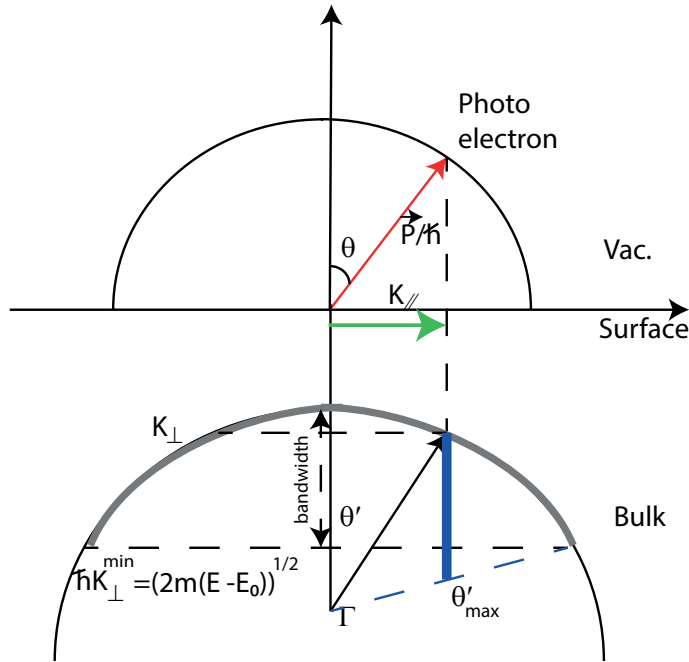


Figure 3: Top part: wavevector of the outgoing photo-electron and its projection, which is conserved for a clean interface. For a surface state, it is the electron wave-vector (green arrow). Bottom, the surface with constant energy is represented for bulk states. There is a range of k_{\perp} momenta perpendicular to the surface which satisfy the conservation of energy and the transverse momentum. As the photon energy is changed this range will vary, changing the intensities maps of the photoemitted spectrum.

On Figure 3, we have represented the electron momenta on each side of the interface. For a bulk bands, there is a range of perpendicular momenta which contribute to the photoelectron intensity which is determined by the band width. When the photon energy is decreased so do the radii of accessible momenta and the range of perpendicular momenta contributing to the photoelectron intensity. For surface electrons, there is only the momentum which matches K_{\parallel} which contribute to a given photo-electron direction (k_{\perp} is undefined because of the interface discontinuity), irrespective of the photon energy used. The dispersion $E_B(K_{\parallel})$ gives the surface band dispersion without any further assumption.

The experimental ARPES spectra of homogeneously strained 100 nm thick HgTe slabs epitaxially grown on [100] CdTe substrates were obtained on the CASSIOPEE line at the SOLEIL synchrotron, whose low energy photons and high resolution (few meV) spectrometer are well suited to topological insulator studies. The strained HgTe slabs were grown by low temperature Molecular Beam Epitaxy in a Ultra-High Vacuum chamber from a [100] CdTe substrate [10]. Only occupied electronic states can be observed in ARPES: indium-doped samples at 10^{18}cm^{-3} were also prepared in addition to the un-doped reference samples, in order to raise the bulk chemical potential. The samples surfaces which spontaneously oxidize in air, were cleaned in a dedicated Ultra High Vacuum preparation chamber by a low-energy Ar-ion sputtering at grazing angles to remove the surface oxide. The *in-situ* LEED spectra observed after surface cleaning (Fig.5) shows a c(2x2) reconstructed pattern consistent with an HgTe [100] growth. The samples were subsequently transferred to the ARPES chamber in Ultra-High Vacuum. The position of the Fermi level was determined with a reference gold sample placed on the same sample holder.

The high-resolution spectra in the vicinity of the Γ -point for an un-doped sample are shown in Fig. 4 [11]. On the left panel a), the intensity of the ARPES spectrum is shown for an incident photon energy $h\nu = 20$ eV. The surface projection of the two volume valence bands $\Gamma_{8,\text{HH}}$ and Γ_6 (deep blue) are observed and, with more intensity (darker), a linear cone structure, which broadens as one moves away from its apex. The second derivative spectrum shown on panel b) enhances the contrast in the ARPES intensity. Within the experimental accuracy the cone apex coincides with the top of the $\Gamma_{8,\text{HH}}$ band and lies 0.1 eV below the Fermi level. On the raw ARPES spectrum shown in panel a) the cone structure extends in the gap with a decreasing intensity, as those states are populated mostly through the room-temperature thermal activation. The cone section for different binding energies shown on the bottom panel are circular up to energies 0.4 eV below the Dirac point. In comparison the heavy hole band $\Gamma_{8,\text{HH}}$ is strongly anisotropic in the $k_x - k_y$ plane.

From the experimental slope of the cone structure, the surface state band velocity is found to be $v_F \approx 5 \times 10^5 \text{m.s}^{-1}$. This value agrees with the lowest order expansion for the energy close to the Dirac point in the Kane model ($\hbar v_F \approx \alpha \frac{P}{\sqrt{6}}$), where the parameter $\alpha \approx 0.9$ for HgTe (the Kane parameters are defined in Ref. [11]). The same sample was also probed at different incident photon energies $h\nu$. We have seen how different incident photon energy shifts the binding energy of bulk bands according to their k_z dispersion. Here, the cone position is unaffected, emphasizing that this cone structure comes from a surface state with no k_z dispersion (see Fig. 5 in [11]). As explained earlier, this is a powerful check which discriminates between 2D and 3D states. Surface state spectra were also collected over the entire Brillouin

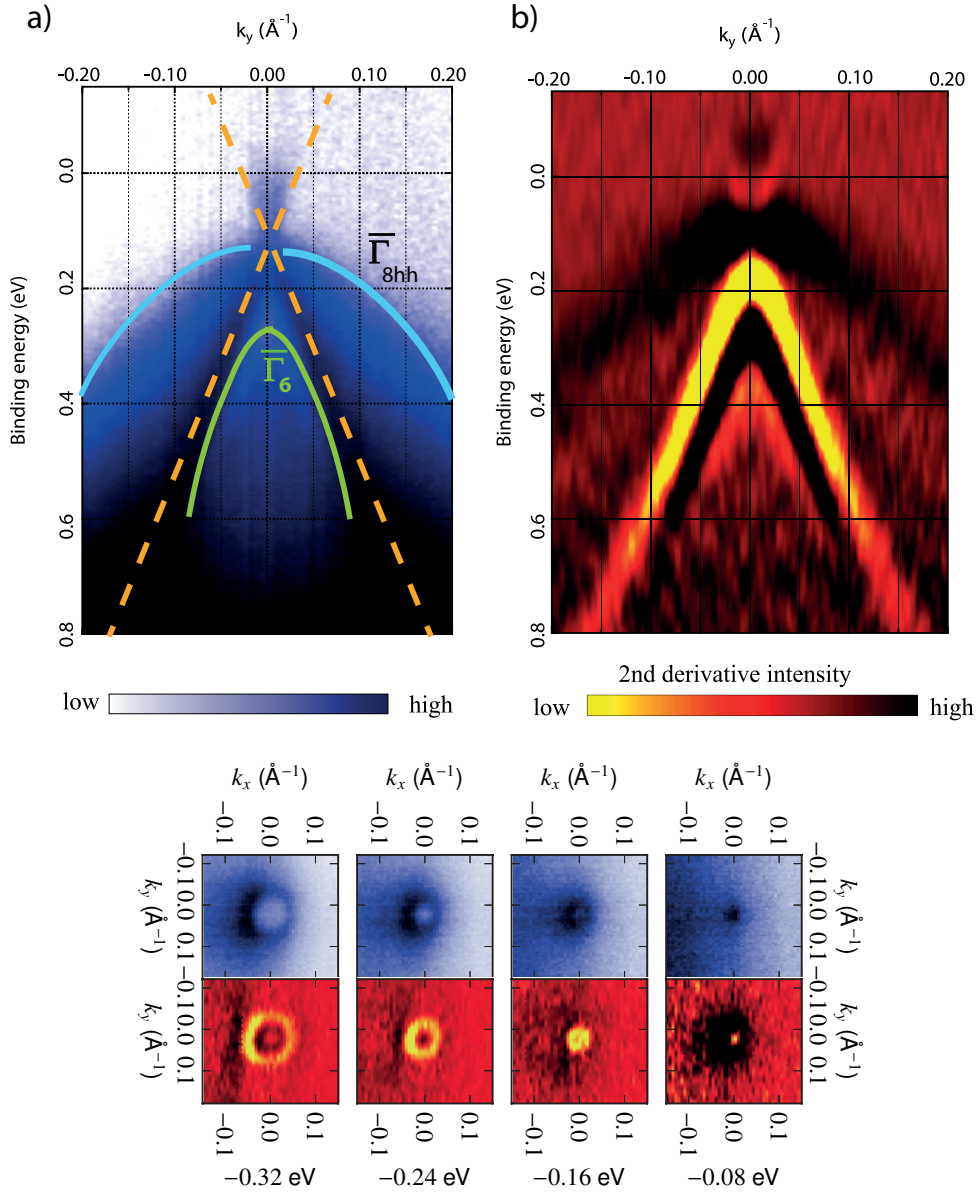


Figure 4: High resolution ARPES spectra for a maximally strained [100] HgTe/vacuum interface in the vicinity of the Γ -point measured at room temperature. a) Energy-momentum intensity spectrum after background subtraction. b) The second derivative of the intensity data enhances the contrast, although band positions are less faithful. Bottom: Intensity spectrum at different energies. The cone structure has a circular section up to ≈ 0.4 eV.

zone. In the Γ -K direction, the surface state spectrum becomes diffuse at energies of 0.8 eV below the Fermi level. On the other hand, in the Γ -X direction, the surface state spectra remain linear all the way to the X point (see Fig. 5), where its energy is 3.4 eV below the Dirac point, i.e. well below the Γ_6 band: in this direction, the surface state robustness goes well beyond the usual topological protection arguments.

This experimental data can be reproduced in great details using the successful Kane model [7], for which all the parameters [12] are known for HgTe. Since we are

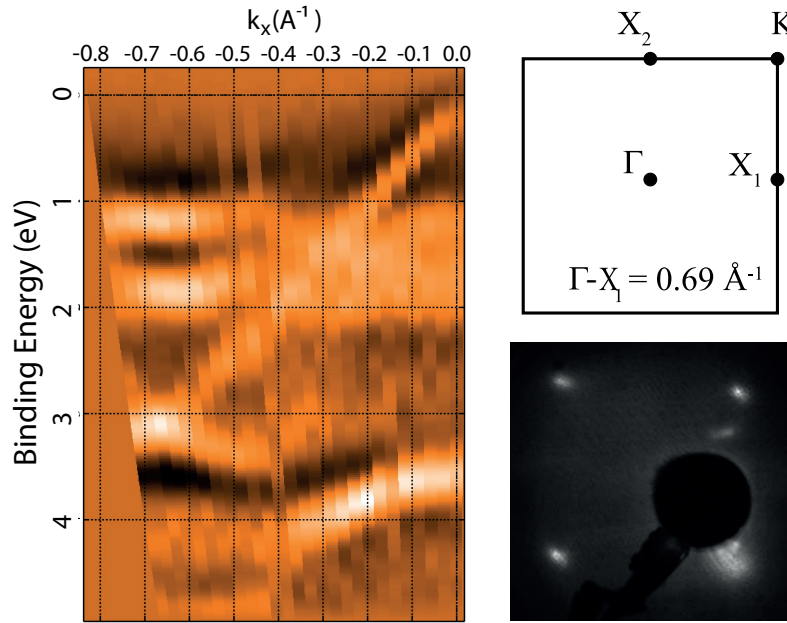


Figure 5: Left: Γ to X_1 ARPES spectrum. The Dirac spectrum observed close to the Γ -point extends all the way to the X point with the same linear slope. Top-right: symmetry points of the Surface Brillouin zone. Bottom-right: LEED pattern observed after low energy Ar^+ surface cleaning: the observed $c(2 \times 2)$ pattern reconstructed surface is in agreement with the half monolayer structures observed on HgTe $[100]$ surfaces.

interested in an inhomogeneous situation where a topological insulator is in contact with a band insulator or vacuum, we discretized the Kane model perpendicular to the interface between an HgTe slab and vacuum with the 6 bands ($\Gamma_{6,\pm 1/2}$, $\Gamma_{8,\pm 3/2,\pm 1/2}$) Kane model. The results are shown to be independent of the discretization constant a over the range of energy and momenta considered. The results are shown in Fig. 6: on the left panel the energy spectrum of all states are represented. The surface states, originating from the inversion between the two $S = \frac{1}{2}$ bands Γ_6 and $\Gamma_{8,\text{LH}}$, are the only states present in the gap. For the Kane parameters used, the energy of the Dirac point is $\epsilon_D = -30 \text{ meV}$ below the $\Gamma_{8,\text{LH}}$ and is similar for a CdTe/HgTe interface. At $k = 0$ (ϵ_D), the surface states do not couple to the $\Gamma_{8,\text{HH}}$ band, and are weakly affected by the $\Gamma_{8,\text{HH}}$ band at small k below ϵ_D . The surface character of the linear spectrum can be verified by projecting the overall surface density over a 5 nm thickness, which is the extension of the surface states at the Dirac point. Their dispersion is linear with the same band velocity as in the experiment. Half of the Dirac cone lies inside the $\Gamma_{8,\text{HH}}$ valence band while the other half continues in the stress gap. When the density is integrated over 1.2 nm , the penetration of the synchrotron radiation, the intensity in the gap decrease, as expected since the penetration of surface states is 5 times larger, a detail which is also observed in the experimental data.

The surface state intensity disappear gradually for larger k , consistent with the observed broadening in the experiment. Their dispersion is linear with the same band velocity as in the experiment.

A hallmark of topological insulators is the helical spin structure of surface states

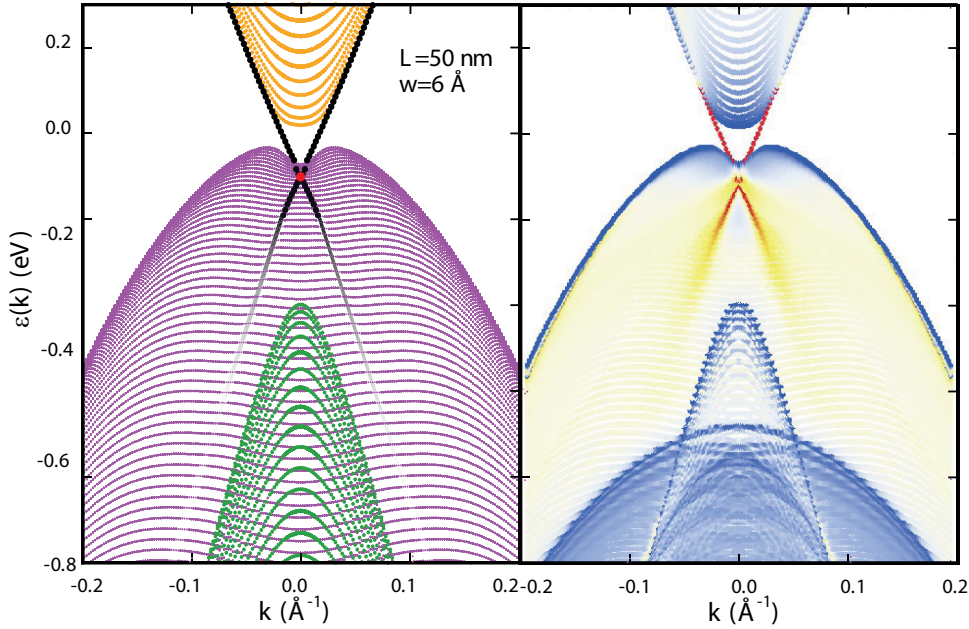


Figure 6: Left: energy spectrum obtained with a inhomogeneous discretized Kane model. One observes in addition to the bulk $\Gamma_{8,LH}$ (orange), $\Gamma_{8,HH}$ (magenta), Γ_6 (green) subbands, a linear dispersive band (black) with a Dirac point 30meV below the top of the $\Gamma_{8,HH}$ valence band. Right: the color-coded electron density at the surface integrated over a 5 nm depth: the broadening observed in the experiment is reproduced by a decrease in surface electron density.

induced by the strong spin-orbit coupling. Such textures have been observed directly using spin-resolved ARPES [13, 14, 15]. This helical spin texture around the surface-states Dirac cone also induces circular dichroism in ARPES, which offers another way to probe this helical spin-texture [16, 17]. Circular dichroism is defined as the asymmetry between the ARPES intensity for left (L) and right (R) circular polarization

$$\mathcal{C}(\epsilon, k) = \frac{I_R(\epsilon, k) - I_L(\epsilon, k)}{I_R(\epsilon, k) + I_L(\epsilon, k)}. \quad (5)$$

It is plotted in Fig. 7 (the geometry is specified in the inset) as a function of k_y for $k_x = 0$ and an incident light beam at $\approx 45^\circ$ with respect to the normal to the sample. By symmetry, the circular dichroism must cancel in the $k_y = 0$ plane as observed for incident photon energies $E_{\text{kin}} > 15.9$ eV.

The most salient features of Fig. 7 are (i) the absence of dichroism from the surface states, signaled by the white lines (no dichroism) along the surface states dispersion and (ii) a significant dichroism (up to 20%) is observed in the bulk $\Gamma_{8,HH}$ band. These results on strained HgTe differ from the circular dichroism ARPES data on Bi_2Se_3 compound [16, 17] where a dominant signature of surface states was observed. The relationship between the circular dichroism and the spectral spin densities of low energy bands is complex and depends on the incident photon energies [18]. On the other hand if we assume that such a relationship exists, Wang et al. [16] have shown that the dependence of the ARPES polarization asymmetry on the band polarizations, $\langle S_x \rangle$ and $\langle S_z \rangle$ is

$$\mathcal{C}(\epsilon, k, \phi) = -a^2 \cos \phi \langle S_z(\epsilon, k) \rangle + 4ab \sin \phi \langle S_x(\epsilon, k) \rangle, \quad (6)$$

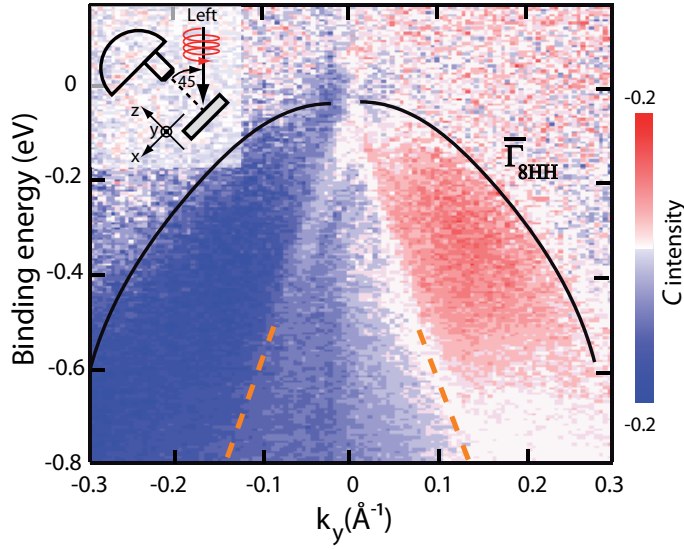


Figure 7: Circular dichroism measured at $k_x = 0 \text{ \AA}^{-1}$. The largest contribution to the dichroism comes from the $\Gamma_{8,HH}$ valence volume band. The surface states appear here as white lines (no dichroism). The inset shows an incident left polarized light beam at 45° with respect to the sample surface.

for a circularly polarized light beam incident in the x - z plane at an angle ϕ with respect to the normal to the sample. The matrix elements a and b depend on surface symmetries of the material [16]. This formula is consistent with the experimental data of Fig.7 if the coefficient b vanishes for the [100] HgTe surface. This explains the weak circular dichroism contribution of the surface states, whose spin polarization normal to the surface $\langle S_z(\epsilon, k) \rangle$ vanishes at low energy. An analysis of the circular dichroism selection rules in ARPES appropriate for the square surface lattice symmetry, confirms that b must vanish at small k . The direct observation of surface states of stressed Mercury Telluride, confirm its topological insulating nature. It has some quite unique features: the Dirac point sits at the top of the heavy hole band. We now turn to their experimental signature in transport experiments.

4 Topological signatures in transport experiments

As seen in the introduction, the Bloch states for the band α in a periodic lattice $|\psi_\alpha(\vec{k})\rangle = e^{i\vec{k}\cdot\vec{R}}u_\alpha(\vec{k})|\vec{R}\rangle$ are phase sensitive. One can construct wavepackets from them and study their semi-classical motion in electric and magnetic field. Topological effects arise from the phase accumulated in a variation of the wavevector \vec{k} in the course of its motion. Just like the Aharonov-Bohm phase, this phase is a line integral of a ‘‘Berry’s’’ vector potential, $\vec{\mathcal{A}}_\alpha(\vec{k}) = i\langle u_\alpha(\vec{k})|\vec{\nabla}_{\vec{k}}u_\alpha(\vec{k})\rangle$. When integrated over a loop \mathcal{C} in \vec{k} within the Brillouin zone, this is an Aharonov-Bohm like phase $\Gamma_{\mathcal{C}} = \oint_{\mathcal{C}} \vec{\mathcal{A}}_\alpha(\vec{k})\cdot d\vec{k}$. Depending on the experimental context, such phase factors are observable in experiments. In a low field magneto-conductance experiment, $\Gamma_{\mathcal{C}}$ affects interference terms at the origin of the localization peak/dip around zero field. In large magnetic field, the motion of charge carriers gets quantized, and this phase affects the quantization condition. In other transport experiments, this term can

be incorporated in the semiclassical equations of motion in the form of an effective magnetic field $\vec{F}(\vec{k}) = \vec{\nabla}_{\vec{k}} \times \vec{\mathcal{A}}_{\alpha}(\vec{k})$ (Berry's curvature) acting on the momentum exactly as a magnetic field does on the position. Explicitly, we define wavepackets from Bloch eigenstates $\psi_{\vec{k}}^{\alpha}(\vec{r}) = e^{i\vec{k} \cdot \vec{R}} u_{\vec{k}}^{\alpha}(\vec{r})$, and compute their center position with the operator $\vec{r} = \frac{\vec{\nabla}_{\vec{k}}}{i} + \vec{\mathcal{A}}(\vec{k})$. The last term introduces a “the shift in the position” which modifies their Poisson brackets $[r_a, r_b] = i\epsilon_{a,b,c} F_c(\vec{k})$. As shown by Haldane [19] and Fuchs [20], this modifies the semiclassical equation of motion,

$$\hbar \frac{d\vec{k}}{dt} = e \left(\vec{E} + \frac{d\vec{r}}{dt} \times \vec{B} \right), \quad (7)$$

$$\hbar \frac{d\vec{r}}{dt} = \vec{\nabla}_{\epsilon_{\alpha}}(\vec{k}) + \hbar \frac{d\vec{k}}{dt} \times \vec{F}(\vec{k}), \quad (8)$$

through the last term in the motion for the position \vec{r} . The Berry's curvature $\vec{F}(\vec{k})$ acts in k -space exactly as a magnetic field does in real space. This $\vec{r} - \vec{k}$ duality can be made more explicit by defining the matrix $J(\vec{k})_{ab}$ as the 2×2 Poisson bracket matrix,

$$J(k)_{ab} = -i \begin{pmatrix} [k_a, k_b] & [k_a, r_b] \\ [r_a, q_b] & [r_a, r_b] \end{pmatrix} = \begin{pmatrix} \frac{e}{\hbar} \epsilon_{abc} B^c & -\delta_a^b \\ \delta_b^a & \epsilon_{abc} F^c(\vec{k}) \end{pmatrix}, \quad (9)$$

and the semi-classical equations of motion take a perfectly dual form

$$\hbar J(\vec{k}) \frac{d}{dt} \begin{pmatrix} r^b \\ q^b \end{pmatrix} = \begin{pmatrix} \nabla_a H(\vec{r}, \vec{k}) \\ \nabla_{k_a} H(\vec{r}, \vec{k}) \end{pmatrix} = \begin{pmatrix} \nabla_a U(\vec{r}) \\ \nabla_{k_a} \epsilon_{\alpha}(\vec{k}) + U(\vec{r}) \end{pmatrix}, \quad (10)$$

where $H(\vec{r}, \vec{k}) = \epsilon_{\alpha}(\vec{k}) + U(\vec{r})$.

Let us first explore the effect of the Berry's flux term $\vec{F}(\vec{k})$ on the quantization condition for a cyclotron orbit in a magnetic field. For this we need to compute the action \mathcal{S} over the closed circular orbit \mathcal{C}

$$\mathcal{S}(\mathcal{C}) eB + \hbar \oint_{\mathcal{C}} \vec{A}(\vec{k}) \cdot d\ell - \pi \hbar = nh. \quad (11)$$

Defining $\Gamma(\mathcal{C}) = \frac{1}{2\pi} \oint_{\mathcal{C}} \vec{A}(\vec{k}) \cdot d\ell$ as Berry's phase orbit, we find

$$\mathcal{S}(\mathcal{C}) \ell_B^2 = n + \frac{1}{2} - \Gamma(\mathcal{C}). \quad (12)$$

For Dirac carriers $\Gamma(\mathcal{C}) = \pm \frac{1}{2}$, depending on the value of the energy with respect to the Dirac point.²

This phase $\Gamma(\mathcal{C})$ can be measured directly using Shubnikov-de Haas oscillations. The resistance maxima in Shubnikov-de Haas oscillations occurs when the chemical potential lies between Landau levels which are full or empty, the broadening coming

²One can show that if a monopole of unit charge is placed at the Dirac point, which is a singularity in the phase of the wavefunctions, $\Gamma(\mathcal{C})$ is the flux of this monopole through \mathcal{C} . Since \mathcal{C} defines a plane dividing the space in two, only half the topological flux is enclosed in \mathcal{C} .

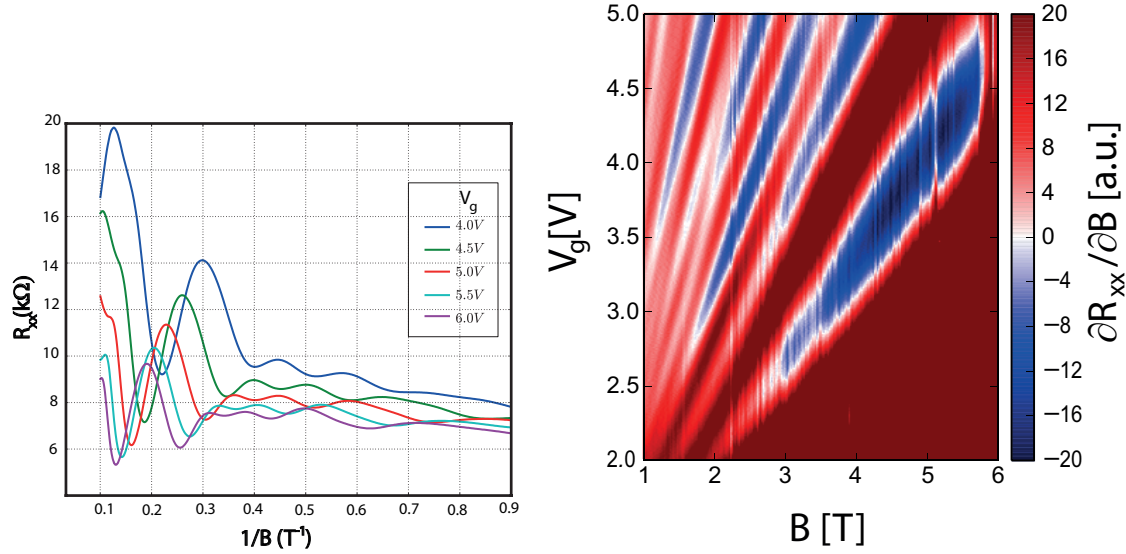


Figure 8: Left: Shubnikov-de Haas oscillations of a gated 100nm thick HgTe sample. As a function of gate voltage, the oscillations period changes. Right: the minima in the Shubnikov de Haas can be located accurately in the V_g - B plane using a color map of the derivative of the longitudinal resistance with respect to the magnetic field. The red and blue zones correspond to a positive and negative slopes, the white line being the extrema. All these extrema converge toward the same gate voltage $V_g \approx 1.3\text{V}$, which we interpret as the chemical potential at the Dirac point.

from disorder or other sources, i.e. they match the minima in the density of states. Gusynin and Shaparov have shown that the conductance oscillation of Dirac-like systems had the form

$$\rho_{xx} = \rho_0(B, T) \cos 2\pi \left(\frac{B_f(\mu)}{B} - \frac{1}{2} + \Gamma \right), \quad (13)$$

where $\rho_0(B, T) = \rho_0 R_D(B, \mu) R(T, \mu)$ includes disorder (Dingle) and thermal broadening factors. The magnetic field frequency $B_f(\mu)$, depends on the value of chemical μ which in the experimental below can be adjusted with an electrostatic gate. The minima of the cosine is reached for values the B_n of B which satisfy

$$2\pi \left(\frac{B_f(\mu)}{B_n} - \frac{1}{2} + \Gamma \right) = 2\pi \left(n - \frac{1}{2} \right), \quad (14)$$

$$\frac{B_f(\mu)}{B_n} = n - \Gamma. \quad (15)$$

In other words for all the values of the chemical potential (gate voltage), the intercept of the minima $\frac{1}{B_n}$ as a function of n gives the value of Γ . On Figure 8, the Shubnikov de Haas oscillations are plotted as a function of magnetic inverse field. The minima in the Shubnikov de Haas oscillations are obtained from the color map shown on the right panel of Fig. 8 and re-plotted as a function of the Landau index in Figure 9. For all gate voltage the straight lines converge to the same intercept on the Landau index axis, which is $\Gamma = \frac{1}{2}$. We see that the topological phase $2\pi\Gamma$ is non-zero and coincide with the π -value expected for Dirac carriers.

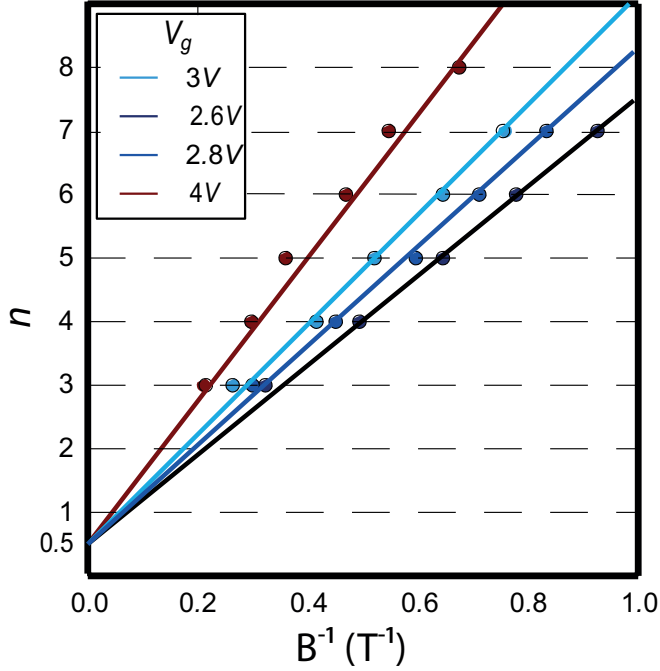


Figure 9: Left: Minima $1/B_n$ in the Shubnikov-de Haas oscillations as a function of the Landau index n . For each gate voltage, the data points lie on a straight line which slope is $B_f(\mu)$ and intercept at 0 is $\Gamma \equiv \frac{1}{2}$.

The Hall conductivity can be computed from the semiclassical equations of motion [19]

$$\sigma_{ab} = \frac{e^2}{h} \epsilon_{abc} \frac{K^c}{2\pi}, \quad \text{where} \quad \frac{K_c}{2\pi} = \left. \frac{h}{e} \frac{\partial n}{\partial B} \right|_{\mu, T=0}. \quad (16)$$

This is Strèda formula. The density n is computed as a the sum over the occupied bands below the Fermi level

$$n = \sum_{\alpha} \int d^2k \det(J(\vec{k})) n_{\alpha}(\vec{k}). \quad (17)$$

The matrix $J_{ab}(\vec{k})$ is defined in Eq. 10, and $\det[J(\vec{k})] = 1 + \epsilon_{abc} \frac{e}{h} B^c F^b(\vec{k})$. For a pure Dirac cone $\partial n / \partial B$ changes sign as the chemical potential crosses the Dirac point giving an ambipolar character to the system as a function of chemical potential. In the ARPES spectra, we saw that there was also an additional source of holes coming from the bulk heavy-hole band $\Gamma_{8, \text{HH}}$. This is illustrated in Figure 10, where the longitudinal resistivity and the tangent of Hall angle normalized by the field are plotted as a function of gate voltage (chemical potential). The tangent of the Hall angle is the ratio between the Hall and the longitudinal resistivity. For a massive band it is $\tan \theta_H = \omega_c \tau = \frac{e\tau}{m} B$. When normalized by the field it is a constant independent of the chemical potential. For Dirac particles, $\tan \theta_H = 2eD_{\mu}^B$, it is inversely proportional to the chemical potential measured with respect to the Dirac point. We see that for increasing gate voltages, the longitudinal resistivity decreases, while the $(\tan \theta_H)/B$ decrease as $1/\mu \propto 1/(V_g - V_{gD})$, which is the behavior expected

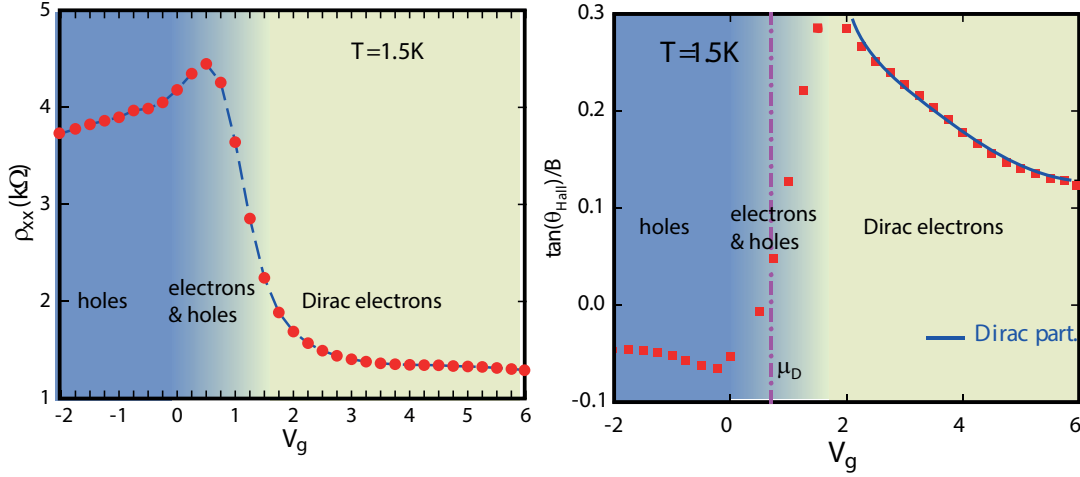


Figure 10: Left: longitudinal resistance as a function of gate voltage. Right: Hall angle as a function of gate voltage. Above $2V$, a $1/(V_g - V_{gD})$ divergence is observed as expected for pure Dirac carriers.

for Dirac electrons. As the gate voltage are decreased, the longitudinal resistivity goes through a maximum and the Hall angle switches sign, indicating that the dominant carriers are holes. At negative gate voltages, the longitudinal resistivity only decreases weakly. This suggest a poor coupling to the bulk heavy-holes which have poor mobilities. This ambipolar character of the electronic transport could also be observed in a semimetal, but the $1/\mu$ dependence of the Hall angle at positive gate voltages is a convincing signature of Dirac-like charge carriers in the gapped region.

The last manifestation of the topological nature of the charge carrier is in the quantum interferences present in the magnetoconductance traces.

A resistance can be expressed as a probability of return to the origin for charge carriers [21]. In two dimensions, this probability depends on closed-loops paths. There are two “time-reversed” directions along which charge particles can travel along each closed loop. For loop sizes smaller than the phase coherence length, the propagation amplitudes add coherently. Depending on their relative phase, this can increase or decrease the probability of return to the origin. For topological insulator surface states, the spin stays perpendicular to the momentum after a scattering event (spin-orbit interactions, see Fig. 11-inset). After the sequence of scattering on a closed loop, the spin has undergone a 2π rotation, which affects the accumulated phase (sign change): For a given loop, the return probability is proportional to $|u_i(\vec{p}, \uparrow) + \Theta u_i(-\vec{p}, \downarrow)|^2$, where Θ represents the time-reverse operation: since $\Theta u_i(-\vec{p}, \downarrow) = -e^{2\pi\Phi/\Phi_0} u_i(\vec{p}, \uparrow)$, the return probability proportional to $\sin^2 2\pi \frac{\Phi}{\Phi_0}$. The sign change comes from the spin rotation and the phase factor $e^{2\pi\Phi/\Phi_0}$ is the accumulated Aharonov-Bohm phase along the loop (Φ is the flux through the loop and $\Phi_0 = h/e$ the flux quantum). We see that the return probability proportional is minimal for zero magnetic field: hence the quantum correction to the conductivity of the Dirac surface states are expected to be *negative*, which is the opposite sign compared to ordinary conductors. Such “anti-localization” quantum corrections to the conductivity have been observed in graphene [22] and other Dirac matter compounds [23] and reveal the presence of a Dirac point [24]. These quantum corrections

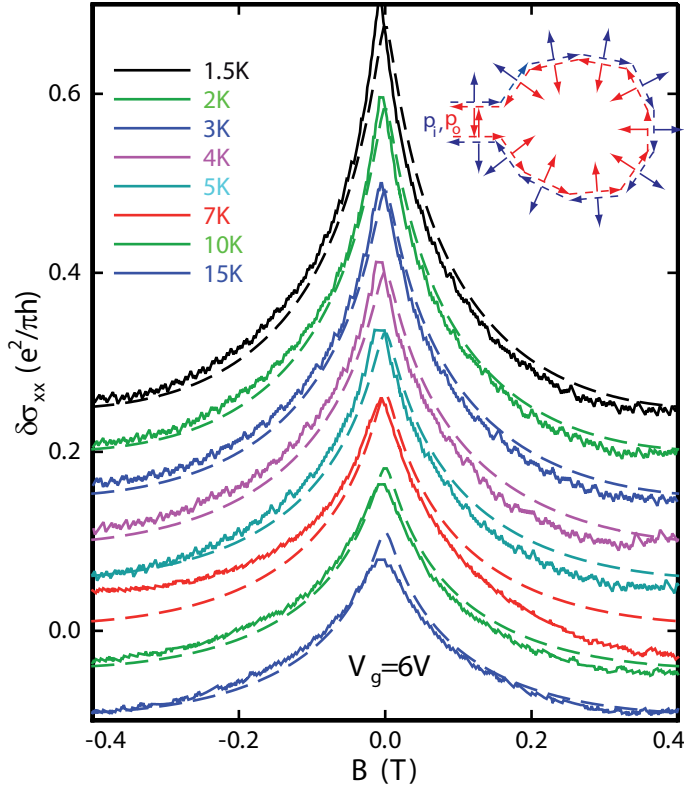


Figure 11: The quantum correction to the conductivity are obtained by subtracting the fit to the measured longitudinal conductivity. The difference are plotted as a function of magnetic field for different temperatures. The curves are fitted to the expected digamma dependence as a function of field. The characteristic field is $B_i = 0.04$ mT $T=1.5$ K and increase with increasing temperature. Beyond B_i , the fitted curves (dotted lines) are dominated by the logarithmic tails expected in 2D.

to the conductivity are obtained by subtracting a fit to the measured longitudinal conductivity and plotted in Fig. 11. Their magnetic field dependence can be fitted to the known dependence [24, 27]. At 1.5 K, the magnitude of the weak-localization correction are ≈ 0.5 times smaller than the expected magnitude $e^2/(2\pi h)$ for a perfect Dirac cone. Only anti-localization corrections are observed, ruling out additional contributions (magnetic impurities). As a function of gate voltage V_g the magnitude of quantum corrections drop by a factor of 2.5 and B_i increase by the same factor as ℓ_{so} is reduced by the population of bulk heavy holes which diffuse the surface states.

5 Conclusions

Topological insulators are a distinct class of materials which differs from ordinary band insulators, by the presence of conducting surface states, which wrap around all the outer surface of the material. This 2D-conducting surface sheet differs from other known 2D electron gases found in semiconducting heterostructures, quantum wells or at the surface of metals, in the energy-momentum dispersion $\epsilon(\vec{k}) = \hbar c|k|$ which is relativistic, i.e. linear in momentum \vec{k} . In addition, the spin of charge carriers are perpendicular to their momentum, giving a helical spin texture on this Dirac cone, a notable difference with graphene, where 2 Dirac cones are presents which have both

possible spin orientations for every momentum.

These surface states have been first studied using angle resolved photoemission (ARPES) and scanning tunnel microscopy (STM), which are powerful surface sensitive probes. These techniques have confirmed the presence of relativistic surface bands, with a helical spin texture. Transport experiments have been successful in material with low bulk conductivity: because of material imperfections, bulk bands often induce a finite conductivity which competes with the surface state contributions. Nevertheless, as materials improves, the typical signature of Dirac carriers are observed in a growing number of experiments.

The helical spin texture of the Dirac cone of topological surface states offers new and interesting scientific perspectives: by selecting the momentum of the carriers, the spin direction is automatically selected. This can be achieved most easily in the spin-Hall regime [25] of 2D topological insulators, where the carriers propagate forward or backward with opposite spin directions at the edge of the 2D structure. Spin filtering [26] and detection using gated H-structures have already been experimentally demonstrated. This spin selection technique with a simple gate offers the possibility to achieve spintronics without the use of magnetic materials.

A final twist which is generating an intense experimental and theoretical effort is the search for Majorana fermions in topological superconductors [2], which can be realized by placing a topological insulator in proximity with an ordinary superconductor. This exciting research goes beyond the topological insulator topic, and gives a new trend in condensed matter science: the combination of materials gives new systems with carefully engineered properties.

References

- [1] Hasan, M. Z., and Kane, C.: *Rev. Mod. Phys.* **82**, 3045 (2010).
- [2] Qi, X.-L., and Zhang, S.-C.: *Rev. Mod. Phys.* **83**, 1057 (2011).
- [3] Fu, L., and Kane, C.: *Phys. Rev. B* **76**, 045302 (2007).
- [4] Shockley, W.: *Phys. Rev.* **56**, 317 (1939).
- [5] Tamm, I.: *Zeitschrift für Physik* **76**, 849 (1932).
- [6] Bernevig, B. A., and Zhang, S.-C.: *Phys. Rev. Lett.* **96**, 106802 (2006).
- [7] Winkler, R.: *Spin Orbit Coupling Effects in Two-Dimensional Electron and Hole Systems*. Springer Tracts in Modern Physics, vol. 191, Springer 2003.
- [8] Bir, G. L., and Pikus, G. E.: *Symmetry and Strain-induced Effects in Semiconductors*. Translated from Russian by P. Shelnitz. Translation edited by D. Louvish. New York, Wiley 1974.
- [9] Damascelli, A.: *Physica Scripta* **T109**, 61 (2004).
- [10] Ballet, P., Thomas, C., Baudry, X., Bouvier, C., Crauste, O., Meunier, T., Badano, G., Veillerot, M., Barnes, J. P., Jouneau, P. H., et al.: *Journal of Electronic Materials* pp. 1–8 (2014).
- [11] Crauste, O., Ohtsubo, Y., Ballet, P., Delplace, P., Carpentier, D., Bouvier, C., Meunier, T., Taleb-Ibrahimi, A., Lévy, L. P.: *Phys. Rev. B* **90** (2014), to appear.

- [12] Novik, E., Pfeuffer-Jeschke, A., Jungwirth, T., Latussek, V., Becker, C., Landwehr, G., Buhmann, H., and Molenkamp, L.: *Phys. Rev. B* **72**, 035321 (2005).
- [13] Hsieh, D., Xia, Y., Wray, L., Qian, D., Pal, A., Dil, J. H., Osterwalder, J., Meier, F., Bihlmayer, G., Kane, C. L., et al.: *Science* **323**, 919 (2009).
- [14] Hsieh, D., Wray, L., Qian, D., Xia, Y., Dil, J. H., Meier, F., Patthey, L., Osterwalder, J., Bihlmayer, G., Hor, Y. S., et al.: *New J. Phys.* **12**, 125001 (2010).
- [15] Kimura, A., Krasovskii, E. E., Nishimura, R., Miyamoto, K., Kadono, T., Kanomaru, K., Chulkov, E. V., Bihlmayer, G., Shimada, K., Namatame, H., et al.: *Phys. Rev. Lett.* **105**, 076804 (2010).
- [16] Wang, Y. H., Hsieh, D., Pilon, D., Fu, L., Gardner, D. R., Lee, Y. S., and Gedik, N.: *Phys. Rev. Lett.* **107**, 207602 (2011).
- [17] Park, S., Han, J., Kim, C., Koh, Y., Kim, C., Lee, H., Choi, H., Han, J., Lee, K., Hur, N., et al.: *Phys. Rev. Lett.* **108**, 046805 (2012).
- [18] Scholz, M. R., Sanchez-Barriga, J., Marchenko, D., Varykhalov, A., Volykhov, A., Yashina, L. V., and Rader, O.: *Phys. Rev. Lett.* **110**, 216801 (2013).
- [19] Haldane, F.: *Phys. Rev. Lett.* **93**, 206602 (2004).
- [20] Fuchs, J. N., Piechon, F., Goerbig, M. O., and Montambaux, G.: *Eur. Phys. J. B* **77**, 351 (2010).
- [21] Montambaux, G.: In *Les Houches Summer School, Session LXXXI*, edited by H. Bouchiat, Y. Gesen, S. Guéron, G. Montambaux, and J. Dalibard, Elsevier, Amsterdam, Vol. 81, 2005.
- [22] Wu, X. S., Li, X. B., Song, Z. M., Berger, C., and de Heer, W. A.: *Phys. Rev. Lett.* **98**, 136801 (2007).
- [23] Chen, J., Qin, H., Yang, F., Liu, J., Guan, T., Qu, F., Zhang, G., Shi, J., Xie, X., Yang, C., et al.: *Phys. Rev. Lett.* **105**, 176602 (2010).
- [24] Kechedzhi, K., McCann, E., Fal'ko, V. I., Suzuura, H., Ando, T., and Altshuler, B. L.: *Eur. Phys. J. Special Topics* **148**, 39 (2007).
- [25] König, M., Wiedmann, S., Brune, C., Roth, A., Buhmann, H., Molenkamp, L. W., Qi, X. L., and Zhang, S. C.: *Science* **318**, 766 (2007).
- [26] Brne, C., Roth, A., Buhmann, H., Hankiewicz, E. M., Molenkamp, L. W., Maciejko, J., Qi, X.-L., and Zhang, S.-C.: *Nat. Phys.* **8**, 485 (2012).
- [27] Tkachov, G., and Hankiewicz, E. M.: Weak antilocalization in HgTe quantum wells and topological surface states: massive versus massless Dirac fermions. *Phys. Rev. B* **84**, 035444 (2011).